Scrape-off layer ion acceleration during fast wave injection in the DIII-D tokamak

D.C. Pace[1], R.I. Pinsker[2], W.W. Heidbrink[3], R.K. Fisher[2], M.A. Van Zeeland[2], G.R. McKee[4], and M. García-Muñoz[5]

[1]Oak Ridge Institute for Science and Education, Oak Ridge, TN 37831-0117, USA
[2]General Atomics, P.O. Box 85608, San Diego, CA 92186-5608
[3]University of California-Irvine, Irvine, CA 92697, USA
[4]University of Wisconsin-Madison, 1500 Engineering Dr., Madison, WI 53706, USA
[5]Max-Planck Institut für Plasmaphysik, Garching D-85748, Germany

E-mail: pacedc@fusion.gat.com

Abstract. Fast wave injection is employed on the DIII-D tokamak as a current drive and electron heating method. Bursts of energetic ions with energy $E_o > 20\,\mathrm{keV}$ are observed immediately following fast wave injection in experiments featuring the 8^{th} ion cyclotron harmonic near the antenna. Using the energy and pitch angle of the energetic ion burst as measured by a fast ion loss detector, it is possible to trace the origin of these ions to a particular antenna. The ion trajectories exist entirely within the scrape-off layer. These observations are consistent with the presence of parametric decay instabilities near the antenna strap. It is suggested that the phase space capabilities of the loss detector diagnostic can improve studies of wave injection coupling and efficiency in tokamaks by directly measuring the effects of parametric decay thresholds.

PACS numbers: 52.35.Mw, 52.20.Dq, 52.40.Fd, 52.50.Qt, 52.55.Fa, 52.70.Nc

1. Introduction

Injection of fast waves at high-harmonic frequencies is a demonstrated method for driving current [1, 2, 3] and heating electrons [4] in tokamak plasmas, and it features promising scalings for reactors [5]. The development of suitable non-inductive current drive is a requirement to achieve steady state operation in ITER [6]. The fast wave system of the DIII-D tokamak [7, 8] is capable of injecting powers of $P_{RF} > 3$ MW into plasmas with either an L-mode or H-mode edge. Reductions in wave heating efficiency are known to occur when particles near the antenna are accelerated and thereby remove energy from the wave before it crosses the boundary of the confined plasma. Particles can be accelerated due to sheath effects (possibly depositing into a nearby surface and leading to sputtering as observed in TFTR [9]) and parametric decay instabilities (in which an ion cyclotron quasi-mode can damp on the perpendicular velocity of cold local ions [10]). A summary of parasitic acceleration mechanisms is found in reference [11]. It is technically difficult to measure plasma processes near the antenna, though electrostatic probes have been successful in proving the existence of parametric decay spectra [12].

This paper presents measurements of energetic ions that are created in the scrape-off layer (SOL) due to high power operation of a fast wave antenna. These measurements are made by a fast ion loss detector capable of resolving the energy and pitch angle of a burst of ions that immediately follow the initial fast wave injection. The simultaneous energy and pitch angle measurement allows for the calculation of the ion orbits. These orbits are traced to an origin near one of the fast wave antennae. The decay of the ion loss signal is consistent with an increasing threshold for parametric decay instabilities close to the antenna strap following an increase in plasma temperature.

Section 2 presents the experimental details, describing the plasma evolution and equilibrium. In section 3, a review of measured energetic ions is presented. Discussion is given in section 4, including the implications of passive fast ion charge exchange measurements (4.1) and the possibility that these ions are accelerated near the antenna

strap by parametric decay instabilities (4.2). Conclusions follow in section 5.

2. Experimental details

The measurements described herein are acquired during an experiment in which fast wave injection is used to directly heat electrons. Figure 1 displays the time evolution of select plasma parameters. An extended plasma current ramp delays the eventual arrival of sawteeth. Flattop current is reached just after $t = 1000\,\mathrm{ms}$, as shown in figure 1(a). This same panel plots the net power from each of the two antennae operated in this discharge. These antennae are described according to their toroidal positions, one at $\phi = 0^\circ$ and another at $\phi = 180^\circ$. The antennae begin injecting at slightly different times. The 180-degree antenna turns on first, beginning at $t = 996.15\,\mathrm{ms}$. It is followed by the 0-degree antenna beginning at $t = 1000.40\,\mathrm{ms}$. During the fast wave heating period there is also neutral beam heating of $P_{NBI} = 5\,\mathrm{MW}$.

Figure 1(b) contains the time evolution of the core electron temperature ($T_e(0)$, from the electron cyclotron emission system [13]), line-averaged electron density ($\bar{n}_e$, from a CO_2 interferometer [14]), and neutron rate (N, from detectors [15]). At $t \approx 1000\,\mathrm{ms}$ there is a significant temperature increase due to a steady 5 MW of neutral beam power and the beginning of fast wave injection. It is within this short time period immediately following the fast wave turn-on that bursts of energetic ions are observed. The electron density and neutron rate display slow increases across $t = 1000\,\mathrm{ms}$ when the input heating is increased. A magnetic equilibrium calculated by EFIT [16] is shown in figure 2. This equilibrium is constrained by magnetic pitch angle measurements from a motional Stark effect system [17]. The fast wave system is set to an injection frequency of $f = 90\,\mathrm{MHz}$ in this discharge, and the resulting deuterium ion cyclotron harmonics are plotted in figure 2 as nearly vertical lines. The neutral gas fill is pure deuterium and only higher-order resonances exist within the plasma. Absorption of fast waves by deuterium beam ions in DIII-D has been studied theoretically and measured experimentally [18, 19, 20, 21]. Measured ion acceleration in the present case is only

observed to occur within the SOL (described in section 3.1) where there is no beam ion population.

Many of the interpretations to follow depend on the toroidal placement of diagnostics and energetic ion production. Figure 3 displays a top-view of DIII-D in which the positions of relevant items are marked. The direction of the toroidal magnetic field (B_T) and plasma current (I_p) for shot 140544 are indicated by the arrows, and these are the most common directions employed in DIII-D discharges. The toroidal extent of the 0-degree and 180-degree fast wave antennae are indicated by rectangles centered on their named positions. For these antennae and the small square indicating the FILD at $\phi = 225°$, the radial incursion of the hardware is exaggerated by the representative shape. The outer circle is positioned at a major radius of $R = 2.379\,\mathrm{m}$. This is the position of the Faraday shield for the fast wave antennae as is labeled $R_{Faraday}$ from this point forward. All of the discharges feature deuterium neutral beams with injection energy $E = 80$ keV and injected power near 5 MW. The co-current injecting beams from shot 140544 are indicated by the dashed lines at $\phi = 30°$ and $330°$ in figure 1.

3. Measurements of energetic ions in the SOL

3.1. Phase space resolved losses measured by FILD

The fast ion loss detector (FILD) [22], based on an existing unit at ASDEX-Upgrade [23], measures the energy and pitch angle of energetic ions that reach its position on the vessel periphery. The FILD is positioned approximately 45° poloidally below the outer midplane as indicated by the ×-symbol in figure 2. This detector is a fast-response scintillator (decay time approximately 490 ns [24]) that emits light due to ion impacts. A collimating slit in the protective shield of the scintillator causes a unique two-dimensional pattern of ion impacts on the scintillator surface. This pattern is a function of ion pitch angle and gyroradius. The term "fast ion losses" is used to describe the measurements of the FILD, but the detected ions in this work are never confined. As will be shown, these ions exist entirely within the SOL as they are generated near the 180-degree antenna

strap and quickly reach the FILD along the outer wall.

Figure 4 is an image from the charge-coupled device (CCD) camera of the FILD immediately following the initial fast wave injection. The camera is 12-bit, leading to a maximum count value of 4095 as shown by the colorbar of the figure. Camera data is acquired at 100 Hz with an exposure time of 4 ms in this shot. The time reported in figure 4 represents the central time of the exposure. For the frame at $t = 1002$ ms, the camera actually acquired light over $1000 \leq t \leq 1004$ ms. While it is possible to operate the FILD with a simultaneously acquired photomultiplier view, this experiment is conducted with only the CCD camera. A large amplitude loss region is observed within the pitch angle range of $55^\circ \leq \alpha \leq 75^\circ$ and gyroradius range of $1.5 \leq r_L \leq 3.0$ cm. A strike map is plotted over the camera image in white. This map is calculated by EfipDesign [25] based on the detector head geometry and the orientation of the local magnetic field. Since the local magnetic field is known, it is also possible to convert the gyroradii values into ion energies. Two of these energy values are shown in the figure as calculated for deuterium. Using the center values of the gyroradius and pitch angle ranges of the observed losses, it is determined that the typical lost ion features an energy of $E_o = 22.4$ keV and pitch angle of $\alpha = 65^\circ$ ($v_\parallel / v = 0.42$).

Figure 5 contains plots of the typical lost ion trajectory as calculated by beginning at the FILD and moving backward in time. The total time elapsed by the displayed orbit trajectory is 55 μs, which is much shorter than any other timescale of interest. Figure 5(a) indicates that this typical ion is never inside of the separatrix. It overlaps with the 8^{th} ion cyclotron harmonic near the outer midplane. The trajectory is plotted all the way to the upper wall, though it is highly unlikely that the energetic ion began this path anywhere near that position. Rather, from the information presented in figure 5(b) it appears the ion was accelerated while passing close to the 180-degree antenna. The displayed orbit is valid from the position at which the ion has been accelerated to its measured energy. The center of this antenna is marked by the intersection of the dashed lines that pass through the vertical midplane and a toroidal position of $\phi = 180^\circ$. Thus,

the FILD is observing energetic ions that are generated at or near the 180-degree antenna strap.

Given that it would be mere chance for the FILD to be positioned such that it measures SOL ions accelerated by a fast wave antenna, an especially critical review of this measurement is performed. This review demonstrates that the FILD observations are not the result of stray light, and that they are consistent with detection of all possible ions accelerated near the 180-degree antenna. The possibility that stray light entered the FILD and produced the pattern shown in figure 4 is ruled out by review of camera data from $t = 302\,\text{ms}$. This time corresponds to the initial neutral beam injection into the colder and lower density early plasma. A bright camera frame results from the large light levels in the plasma edge. The collimating aperture is displaced (upper-left in the orientation of figure 4) such that stray light reaches the lowest pitch angle side of the scintillator, in contrast to the larger pitch angle losses at $t = 1002\,\text{ms}$. Count rates during this early burst of plasma light reach maximum values of approximately 2500 and are much lower than the saturated 4095 count value measured during the initial fast wave injection.

A review of all the detectable FILD orbits shows that the measured pattern of figure 4 includes nearly all of the ion phase space that could possibly reach the FILD after beginning near the 180-degree antenna. Modeling is performed by calculating an ion trajectory for each intersection point of the strike map in figure 4. Each trajectory is then classified according to whether it may have originated from the 180-antenna. The contour of these orbit types is given in figure 6(a). The $\diamond$-symbol indicates trajectories that are clearly capable of reaching the FILD and overlap with the wall and 8^{th} ion cyclotron harmonic at the outer midplane. The colors of the contour fill in the space between symbols of the same designation. Ions that can reach the FILD, but that pass the outer midplane inside of the separatrix, are indicated by the +-symbol. Orbit trajectories that approach very near to the bottom tiles are designated by the *-symbol. These ions may originate near the 180-degree antenna, but they are likely to strike the

outer wall away from the FILD. Those that certainly strike the bottom tiles and could not have originated from the 180-degree antenna are marked with □-symbols. Points of phase space that do not show up on the strike map of figure 4 are marked with ×-symbols. Example trajectories from the marginal, bottom striking, and inside-separatrix classifications are shown in figure 6(b).

The modeled phase space of the contour in figure 6(a) is very similar to the measured loss space shown in figure 4. In both cases, the most densely populated region occurs for pitch angles above 50 degrees and the lower half of the gyroradius range. Furthermore, the gyroradius range extends to larger values with increasing pitch angle. This is consistent with the measurement that shows the loss region extending to larger gyroradii along the 70 degree pitch angle line. This orbit modeling also allowed for the determination, using an established FILD analysis [26], that none of the FILD phase space is populated by prompt losses from the co-current injecting neutral beams that are used during the time of initial fast wave injection. There are three areas of phase space for which this modeling and the measurements appear to contrast. One region of apparent disagreement between the modeled and measured phase space is the $\alpha > 73$ degree region for which the model indicates possible losses but none are measured. These ion trajectories are calculated to originate from the outer wall near the bottom of the antenna structure, possibly too low to be produced by the antenna. A second possible region of disagreement occurs for the larger gyroradius range of $r_L \geq 3\,\mathrm{cm}$. The modeling presented in figure 6 does not produce information concerning the expected number density of losses, however, so any measured loss flux is consistent. There are measured losses for this gyroradius range shown in figure 4, and those signal levels are simply reduced compared to the saturated camera pixels for the smaller gyroradii. Finally, there are no measured losses at the lowest energy and highest pitch angle region as identified in figure 6(a). Ions within that phase space have a clear path to the FILD, suggesting that the lack of observed losses is due to a particular feature of the acceleration mechanism near the antenna.

A time history of ion losses, calculated by taking the average FILD camera count for a given region in each frame, is shown in figure 7(a). Injected powers from the 180-antenna and the neutral beams are plotted in figure 7(b) along with the edge electron temperature, $T_e(a)$, from the ECE diagnostic. These are the same power traces as shown in figure 1(a), though they are smoothed for this extended time range display. The inset of figure 7(a) indicates the region of interest as defined within the frame at $t = 1002$ ms shown in figure 4. This region of interest does not always enclose the same range of pitch angles and gyroradii within a single shot because of the changing map during the plasma current ramp. The increased loss levels prior to $t = 1000$ ms are attributed to the upper null plasma shape that places the separatrix closer to the FILD than is the case during standard lower null shapes; these losses decrease as the plasma current increases and energetic ion confinement improves. The same two neutral beams are injecting through $t = 2000$ ms, only their pulse timing is changed. The fast ion loss produced by these beams has decreased to a minimal level by $t = 1000$ ms when the fast wave injection begins. The burst of losses that coincide with the initial injection of fast wave energy at 1000 ms causes a full saturation of this region of phase space. This is nearly twice the signal level of losses occurring during the current ramp when energetic ion confinement is known to be reduced. The decay from this burst is slightly slower than the decay observed following $t = 500$ ms. The decaying loss signal is consistent with an increasing parametric decay threshold due the rising edge temperature as seen in figure 7(b). The actual threshold depends on additional plasma parameters and is discussed in section 4.2. An increased threshold, though not one due entirely to the electron temperature, may also explain the reduced level of losses that are observed in subsequent fast wave injections as shown for $t > 2000$ ms in figure 7(a).

3.2. Loss dependencies

Qualitatively similar bursts of energetic ions are observed on all discharges featuring fast wave injection during this experiment. A single magnetic equilibrium is used, and

the FILD measures no losses after $t = 1000$ ms during shots in which no fast wave injection is applied. Figure 8 displays a FILD camera frame from $t = 1012$ ms during shot 140539. A gold rectangle encloses the region of phase space that is analyzed across all fast wave shots from this experiment. During this shot, the 180-degree antenna operated at slightly over 1 MW net power. That increased power level may explain the larger loss signal occurring at larger gyroradii as compared to the frame shown in figure 4.

Figure 9(a) is a plot of the energetic ion loss (total number of counts) as a function of net power of the 180-degree fast wave antenna, $P_{180-deg}$. The value of $P_{180-deg}$ is calculated by averaging over the time windows corresponding to the exposure period of the FILD camera. Only frames acquired between $990 \leq t \leq 1200$ ms are analyzed, and error bars represent statistical error. Oversized *-symbols represent values calculated using only the FILD frame at $t = 1002$ ms. This is the first frame following turn-on of the 180-degree antenna. From figure 9(a) it appears as though the loss production is subject to a threshold in antenna power. There is little to no change in the loss signal up to $P_{180-deg} \approx 0.4$ MW, and these levels likely represent the noise floor since no beam prompt-losses exist in this phase space region. The trend in bremsstrahlung (continuum) emission [27] is plotted in figure 9(b) for comparison with the ion loss signal. From a simple conceptual viewpoint, this signal may be indicative of outgassing from all antennae and is therefore not expected to scale in the same way as the ion loss signal from a single antenna. The bremsstrahlung emission scales nearly linearly with 180-degree antenna power.

4. Discussion

4.1. Passive FIDA measured by beam emission spectroscopy

An attempt is made to observe light emitted by ions at the 180-degree antenna using a beam emission spectroscopy system without neutral beam injection. The energetic ion emission is found to be below the bremsstrahlung emission along the sightlines of

the diagnostic. It has recently been demonstrated that beam emission spectroscopy (BES) systems are capable of detecting fast ion D_α (FIDA) light [28] that is generated passively in the SOL. Passive generation denotes the emission of light due to charge exchange processes between energetic ions and background neutrals (active generation occurs when the neutral particle is injected by a beam). The ability of the DIII-D BES system [29] to detect the presence of energetic ions has recently been demonstrated [30]. In typical geometry, the fast-ion BES signal is dominated by ions of energy $E_o > 20\,\mathrm{keV}$ over a wavelength range of approximately $651 \leq \lambda \leq 655\,\mathrm{nm}$, where the unshifted D_α line occurs at 656.1 nm.

The toroidal positions of many BES sightline terminations lie on the 180-degree fast antenna. Figure 10 shows the toroidal position where each BES sightline reaches the major radius position of the antenna's Faraday shield ($R_{Faraday} = 2.379\,\mathrm{m}$). Horizontal lines mark the toroidal extent of the antenna structure ($\Delta\phi \approx 18°$). These sightlines should be expected to observe fast ion generation at the antenna. An example of the passive BES signal during shot 140544 is shown in figure 11(a). Changes in this signal are observed to coincide with neutral beam injection from beams that do not intersect the sightlines. Neutral beam injection begins at $t = 300\,\mathrm{ms}$ and causes increased BES signal that decays to a steady value after a few hundred milliseconds. The beginning of fast wave injection at $t = 1000\,\mathrm{ms}$ increases the BES signal level further (the beam power adjustment at this time contributes little to no change in the BES signal). Sawtooth crash modulation of the signal is seen during $2300 \leq t \leq 3300\,\mathrm{ms}$. Just prior to $t = 3500\,\mathrm{ms}$ there is a brief injection from the 180-degree fast wave antenna during a period of reduced neutral beam power that further demonstrates the effect from this antenna alone. In all cases, the BES signal is similar in relative evolution to the Bremsstrahlung chords that are placed near the outer midplane.

Figure 11(b) quantifies the increase in BES signal due to the injection of the 180-degree antenna. The change in signal, Δ_{BES}, is calculated according to the following

expression,

$$\begin{aligned} S_{norm} = &\quad \frac{S - S_{off}}{S_{max}} \quad , \\ \Delta_{BES} = &\quad S_{norm}(t = 1000) - S_{norm}(t = 996) \quad , \end{aligned} \tag{1}$$

where S is the BES data from the time range $990 \leq t \leq 1020$ ms, S_{off} is the offset value of this set, S_{max} is the maximum value, and the time values are in milliseconds. Given the injection times of the fast wave antennas (180-degree at 996.15 ms and 0-degree at 1000.40 ms), the value of Δ_{BES} represents the relative increase in BES signal due to the initial injection of the 180-degree antenna. Figure 11(b) shows that channels located within the toroidal extent of this antenna typically exhibit increases greater than 15%. Channels that terminate further away from the antenna at $\phi > 190°$ demonstrate a trend of steady decline in Δ_{BES}. This trend, by itself, is consistent with either the BES signal being dominated by Bremsstrahlung from antenna outgassing or resolving a contribution from fast ions near the antenna.

Passive FIDA light collected by the BES system is from a different region of phase space compared to the FILD. The BES spectral range is on the blue-shifted side of the cold D_α line. Following the method of [30], the phase space sensitivity of the BES measurement is calculated and shown in figure 12. This normalized phase space weighting, W_{BES}, is calculated for the portion of the BES sightline that terminates near the 180-degree fast wave antenna. The orientation of $v_\parallel/v$ is such that positive values represent co-current traveling ions, as is the case in the FILD analysis. The BES measurement bears almost no influence from energetic ions that are traveling counter-current near their creation at the antenna. This is exactly opposite to the measured phase space of the FILD, which requires ions to be counter-propagating at the antenna so they connect to the FILD on the outer, co-current leg of their orbits. The ion trajectory of figure 5 is used to determine the pitch near the antenna and this is marked on the weight function contour of figure 12. Ions observed by the FILD make no contribution to the BES signal level. The interpretation of these observations is either that the bremsstrahlung emission is at all times greater than the passive FIDA emission, or that

the ion acceleration mechanism was not populating the phase space in which the BES system is sensitive.

4.2. Parametric decay instabilities as the production mechanism

The energetic ion losses observed by the FILD are consistent with ion acceleration occurring near the 180-degree antenna strap due to the presence of parametric decay instabilities (PDI). A definitive study of this possibility will necessarily include probes placed near the antenna to measure PDI spectra, along with full SOL plasma profiles. As that is not available in the present treatment, a discussion concerning PDI effects is given here, and the design of a new experiment is presented in section 5. The first measurements of parametric decay instability in the SOL were achieved in ion cyclotron range of frequencies (ICRF) heating experiments on ASDEX [12]. These include the detection of two PDI processes: (1) injected wave decays into an ion Bernstein wave (IBW) and an ion cyclotron quasimode, and (2) injected wave decays into an IBW and an electron quasi-mode. No energetic ion measurements were included in this work, though their production in the SOL was posited. Acceleration of edge ions up to $E = 5.6\,\mathrm{keV}$ was observed [31] in JT-60 during ICRF heating. Parametric decay instabilities were measured and one of the processes included the production of an IBW and an ion cyclotron quasimode. The SOL fast ions were produced when the toroidally-displaced antenna straps were in phase. When the antenna straps had a toroidal phasing of 180 degrees there was no observed edge fast ion generation. Multiple ICRF harmonic peaks produced through PDI have also been observed [32] on TEXTOR. Additional sideband modes at impurity cyclotron harmonics were measured. Though fast ions in the SOL were not measured, heat flux to the limiters and impurity generation observations provided for a conclusion that ICRF energy was directly absorbed by SOL ions. The energy deposited in the SOL in this case was of the order 5%.

Many measurements of SOL generated fast ions have been made with neutral particle analyzers. This provides a wealth of information concerning ion energies,

but limited information concerning pitch angles and time evolution. Acceleration of SOL ions during ion Bernstein wave heating was observed [33] in DIII-D. This was linked to PDI with the various ion cyclotron harmonics measured by an electrostatic Langmuir probe. The largest PDI signal was measured when the antenna frequency was approximately twice the hydrogen cyclotron frequency near the antenna, i.e., $\omega_{\mathrm{RF}} \approx 2\Omega_{\mathrm{H}} = 4\Omega_{\mathrm{D}}$. The PDI process involves the conversion of the antenna-injected electron plasma wave into an IBW and an ion cyclotron quasimode. Neutral particle analyzer measurements of fast ions were acquired in these discharges. Peak measured energies were $E_{\mathrm{H}} \approx 25\,\mathrm{keV}$ ($T_{\mathrm{tail}} = 5.5$ keV) and $E_{\mathrm{D}} \approx 15\,\mathrm{keV}$ ($T_{\mathrm{tail}} = 1.8\,\mathrm{keV}$) for hydrogen and deuterium, respectively. Energetic ions of $E_o > 5\,\mathrm{keV}$ were found [34] to originate in the SOL during ICRF heating in Alcator C-Mod. The detection of fast ions occurred on time scales faster than the best resolution of the neutral particle analyzer diagnostic ($\Delta t = 100\,\mu\mathrm{s}$) at both ICRF turn-on and turn-off. This time behavior indicated that the fast ions must originate in the SOL where the confinement time is shorter than the observed response. The maximum energy observed was 50 keV. In the case of hydrogen minority ICRF heating, a theoretical model found that the threshold RF electric field to achieve PDI increased with SOL electron temperature [35].

While the situation is more complicated when an ion cyclotron harmonic resides near the antenna, it is possible that the decay in FILD measured ion loss is partly due to the rapidly increasing electron temperature (the core increase is shown in figure 1). Power thresholds for PDI have been determined theoretically in multi-species plasmas [36]. The ability to increase this threshold and thereby reduce PDI has been demonstrated in the case of lower-hybrid injection [37]. High-harmonic fast wave (HHFW) heating is applied on NSTX and the IBW resulting from PDI leads to a measurable increase in ion temperature over the confined plasma edge [38]. The HHFW power threshold to produce a PDI spectrum was observed to be $P = 0.65$ MW.

Experimental observations up to this point encouraged a theoretical work [39] that determined ion cyclotron turbulence cannot be responsible for transferring significant

energy to SOL ions. That work showed short wavelength modes could be excited at an antenna, but are not relevant for studying SOL fast ions. Taken together, the existing body of work concerning the acceleration of SOL ions by PDI is consistent with the measured energy of SOL ions in this work. The previously referenced DIII-D study of fast wave injection [18] observed PDI during 8th harmonic heating. That work speculated that PDI might be stronger in 8^{th} harmonic operation compared to 4^{th} harmonic. No edge fast ion measurements were presented.

5. Conclusions and future work

Bursts of energetic ions are observed to originate from a region near a fast wave antenna at DIII-D. In this instance, the magnetic equilibrium is such that the 8^{th} ion cyclotron harmonic resides near the antenna. The energy and pitch angle of these ions is measured by a fast ion loss detector (FILD). Orbit trajectories from the FILD intersect the near fields of the 180-degree fast wave antenna and remain entirely within the SOL. The measured energetic ion signal peaks rapidly following fast wave turn-on and then decays. The range of gyroradii and pitch angles of the FILD-measured ions are well modeled.

The decay of the energetic ion loss signal is consistent with an increasing threshold for parametric decay instabilities near the antenna. The minimum antenna power to produce a PDI spectrum is known to increase with SOL electron temperature. The full dependencies, to the extent they are known or have been measured, are complicated functions of magnetic field, density, ion temperature, and impurity concentration. A future DIII-D experiment is proposed that will utilize the plasma equilibrium shown here, and complimented by additional PDI-relevant diagnostics. Edge reflectometry is capable of providing electron density well into the SOL. Electrostatic probes have been used previously to identify PDI spectra near antennae. Additional Langmuir probes will measure SOL electron temperature. The combined results allow for determination of PDI thresholds, while the FILD measurement characterizes the energy transfer to energetic ions. It is not required that SOL ion acceleration follow the appearance of a

single PDI harmonic, so the finely resolved phase space capability of the FILD has the potential to contribute uniquely to the understanding of this parasitic process.

Finally, these results indicate the value of diagnostics with three-dimensional resolution. The particular relative placement between the FILD and the fast wave antenna enabled the detection of ion acceleration at the antenna. A distributed set of FILDs should be particularly useful for a variety of non-axisymmetric ion loss generating effects in present experiments, e.g., those occurring from the magnetic perturbations of test blanket modules [40].

Acknowledgments

The work of DCP was supported by the US Department of Energy through an appointment in the Fusion Energy Postdoctoral Research Program and the US Department of Energy under DE-FC02-04ER54698, SC-G903402, DE-FG02-89ER53296, and DE-FG02-08ER54999. The authors would like to thank S.J. Wukitch and C. Rost for discussing parametric decay instabilities and A.E. White for supporting piggyback FILD operation during fast wave experiments. In addition, the authors are grateful to M.E. Austin and N.H. Brooks for providing supporting data, and to C.C. Petty and X. Chen for reading a draft manuscript.

References

[1] Pinsker R.I., Petty C.C., Porkolab M., Baity F., Bonoli P., Callis R.W., Cary W.P., Chiu S.C., Freeman R.L., Goulding R., deGrassie J.S., Harvey R.W., Hoffman D., James R., Kawashima H., Luce T.C., Mayberry M., Prater R. and the DIII-D Team 1992 *Fourteenth Conference Proceedings of the IAEA Conference on Plasma Physics and Controlled Fusion Research (i.e., Fusion Energy Conference), Würzburg, Germany*, Vol. 1, p. 683 paper IAEA-CN-56/E-2-4 URL `http://www-naweb.iaea.org/napc/physics/FEC/STIPUB906_VOL1.pdf`

[2] Petty C.C. *et al* 1995 *Nucl. Fusion* **35** 773

[3] Porkolab M. *et al* 1998 *Plasma Phys. Control. Fusion* **40** A35

[4] Petty C.C. *et al* 1992 *Phys. Rev. Lett.* **69** 289

[5] Ono M. 1995 *Phys. Plasmas* **2** 4075

[6] Gormezano C. *et al* 2007 *Nucl. Fusion* **47** S285

[7] Luxon J.L. 2002 *Nucl. Fusion* **42** 614

[8] Greenfield C.M. and the DIII-D Team 2011 *Nucl. Fusion* **51** 094009

[9] D'Ippolito D. *et al* 1998 *Nucl. Fusion* **38** 1543

[10] Myra J., D'Ippolito D., Russell D., Berry L., Jaeger E. and Carter M. 2006 *Nucl. Fusion* **46** S455

[11] Heikkinen J., Rantamki K., Karttunen S., Lampela A., Mantsinen M. and Pttikangas T. 2000 *Contrib. Plasma Phys.* **40** 276

[12] Nieuwenhove R.V., Oost G.V., Noterdaeme J.M., Brambilla M., Gernhardt J. and Porkolab M. 1988 *Nucl. Fusion* **28** 1603

[13] Austin M.E. and Lohr J. 2003 *Rev. Sci. Instrum.* **74** 1457

[14] Van Zeeland M.A., Boivin R.L., Carlstrom T.N., Deterly T.M. and Finkenthal D.K. 2006 *Rev. Sci. Instrum.* **77** 10F325

[15] Heidbrink W.W., Taylor P.L. and Phillips J.A. 1997 *Rev. Sci. Instrum.* **68** 536

[16] Lao L.L., St John H., Stambaugh R.D., Kellman A.G. and Pfeiffer W. 1985 *Nucl. Fusion* **25** 1611

[17] Holcomb C.T., Makowski M.A., Jayakumar R.J., Allen S.L., Ellis R.M., Geer R., Behne D., Morris K.L., Seppala L.G. and Moller J.M. 2006 *Rev. Sci. Instrum.* **77** 10E506

[18] Pinsker R.I. *et al* 2006 *Nucl. Fusion* **46** S416

[19] Choi M., Chan V.S., Pinsker R.I., Petty C.C., Chiu S.C., Wright J., Bonoli P. and Porkolab M. 2006 *Nucl. Fusion* **46** S409

[20] Heidbrink W.W., Luo Y., Burrell K.H., Harvey R.W., Pinsker R.I. and Ruskov E. 2007 *Plasma Phys. Control. Fusion* **49** 1457

[21] Mantsinen M.J., Petty C.C., Eriksson L.G., Mau T.K., Pinsker R.I., and Porkolab M. 2002 *Phys. Plasmas* **9** 1318

[22] Fisher R.K., Pace D.C., García-Muñoz M., Heidbrink W.W., Muscatello C.M., Van Zeeland M.A. and Zhu Y.B. 2010 *Rev. Sci. Instrum.* **81** 10D307

[23] García-Muñoz M., Fahrbach H.U., Zohm H. and the ASDEX Upgrade Team 2009 *Rev. Sci. Instrum.* **80** 053503

[24] García-Muñoz M. 2006 *Fast Response Scintillator Based Detector for MHD-Induced Energetic Ion Losses in ASDEX Upgrade*, Ph.D. thesis Ludwig-Maximilians-Universität München

[25] Werner A., Weller A., Darrow D.S. and W7-AS Team (W7-AS Team) 2001 *Rev. Sci. Instrum.* **72** 780

[26] Pace D.C., Fisher R.K., García-Muñoz M., Darrow D.S., Heidbrink W.W., Muscatello C.M., Nazikian R., Van Zeeland M.A. and Zhu Y.B. 2010 *Rev. Sci. Instrum.* **81** 10D305

[27] Schissel D.P., Stockdale R.E., St John H. and Tang W.M. 1988 *Phys. Fluids* **31** 3738

[28] Heidbrink W.W., Burrell K.H., Luo Y., Pablant N.A. and Ruskov E. 2004 *Plasma Phys. Control. Fusion* **46** 1855

[29] McKee G., Ashley R., Durst R., Fonck R., Jakubowski M., Tritz K., Burrell K., Greenfield C. and Robinson J. 1999 *Rev. Sci. Instrum.* **70** 913

[30] Heidbrink W.W., McKee G.R., Smith D.R. and Bortolon A. 2011 *Plasma Phys. Control. Fusion* **53** 085007

[31] Fujii T. *et al* 1990 *Fusion Eng. Design* **12** 139

[32] Oost G.V. *et al* 1990 *Fusion Eng. Design* **12** 149

[33] Pinsker R.I., Petty C.C., Mayberry M.J., Porkolab M. and Heidbrink W.W. 1993 *Nucl. Fusion* **33** 777

[34] Rost J.C., Porkolab M. and Boivin R.L. 2002 *Phys. Plasmas* **9** 1262

[35] Rost J.C. 1998 *Fast Ion Tails during Radio Frequency Heating on the Alcator C-Mod Tokamak*, Ph.D. thesis Massachusetts Institute of Technology

[36] Porkolab M. 1990 *Fusion Eng. Design* **12** 93

[37] Uehara K. *et al* 1982 *Nucl. Fusion* **22** 428

[38] Wilson J.R., Bernabei S., Biewer T., Diem S., Hosea J., LeBlanc B., Phillips C.K., Ryan P. and Swain D.W. 2005 *AIP Conf. Proc.* **787** 66

[39] Mikhailenko V.S. and Scime E.E. 2004 *Phys. Plasmas* **11** 3691

[40] Schaffer M.J. *et al* 2011 *Nucl. Fusion* **51** 103028

LIST OF FIGURE CAPTIONS

Figure 1. (Color) Time evolution of parameters from shot 140544. (a) Plasma current (I_p) and net power from the 0-degree (P_{0-deg}) and 180-degree ($P_{180-deg}$) fast wave antennae. (b) Central electron temperature [$T_e(0)$], line-averaged electron density ($\bar{n}_e$), and neutron rate (N).

Figure 2. (Color online) Magnetic equilibrium from shot 140544 at $t = 1005\,\mathrm{ms}$. The nearly vertical lines represent deuterium cyclotron harmonics given the $f = 90\,\mathrm{MHz}$ injection frequency of the fast wave system.

Figure 3. (Color online) Top view of DIII-D indicating the toroidal positions of the fast wave antennae ($\phi = 0°, 180°$), the FILD ($\phi = 225°$), and the co-current injecting neutral beams (NBI at $\phi = 30°, 330°$). Sightline extrema from the BES system are shown in red.

Figure 4. (Color online) Camera image from the FILD CCD during the first frame acquired following fast wave injection.

Figure 5. (Color online) (a) Rz-projection of an ion trajectory detected by the FILD. The deuterium ion features an energy of $E_o = 22.4\,\mathrm{keV}$ and a pitch angle at the FILD of 65 degrees ($v_\parallel/v = 0.42$). (b) ϕz-projection of the detected ion orbit. Dashed lines represent the vertical midplane and a toroidal position of $\phi = 180°$.

Figure 6. (Color online) (a) Phase space map of orbit trajectory for all possible orbits detectable by the FILD during shot 140544 at 1005 ms. Orbits are classified as those that: may originate at the 180-degree antenna ($\diamond$), exist within the separatrix on the outer midplane (+), are marginally detectable as they may have hit the bottom of the vessel (*), clearly hit the bottom of the vessel ($\square$), do not appear on the strike map ($\times$). (b) Magnetic equilibrium from shot 140544 at 1002 ms with example trajectories of the marginal (*, $\alpha = 60°$, $r_L = 1.5\,\mathrm{cm}$), bottom striking ($\square$, $\alpha = 40°$, $r_L = 4.5$ cm), and inside separatrix (+, $\alpha = 65°$, $r_L = 4.0\,\mathrm{cm}$) orbits.

Figure 7. (Color online) (a) Time evolution of the average FILD camera count within a region of interest as indicated by the inset. (b) Injected power from the neutral beams and 180-degree antenna along with edge electron temperature.

Figure 8. (Color online) FILD camera frame at $t = 1012\,\text{ms}$ during shot 140539. The gold rectangle enclosing all gyroradii and centered on the 70° pitch angle region represents the analysis region applied across all shots of interest.

Figure 9. (Color) (a) Ion loss signal (total number of counts) within the FILD camera region identified in figure 8, and (b) bremsstrahlung (continuum) emission as a function of net power from the 180-degree antenna, $P_{180-deg}$.

Figure 10. (Color online) Toroidal angle where each BES sightline intersects the fast wave antenna Faraday shield ($R_{Faraday} = 2.379\,\text{m}$).

Figure 11. (Color) (a) BES (ch. 32) time trace compared to fast wave antenna and neutral beam injected powers in shot 140544. (b) Normalized change in the BES signal, Δ_{BES}, as a function of the toroidal position where the sightline terminates ($R_{Faraday} = 2.379\,\text{m}$).

Figure 12. (Color online) Normalized phase space sensitivity, W_{BES}, of a typical BES sightline that intersects near the 180-degree fast wave antenna. The ⋄-symbol marks the property of the FILD measured ion as shown in figure 5.

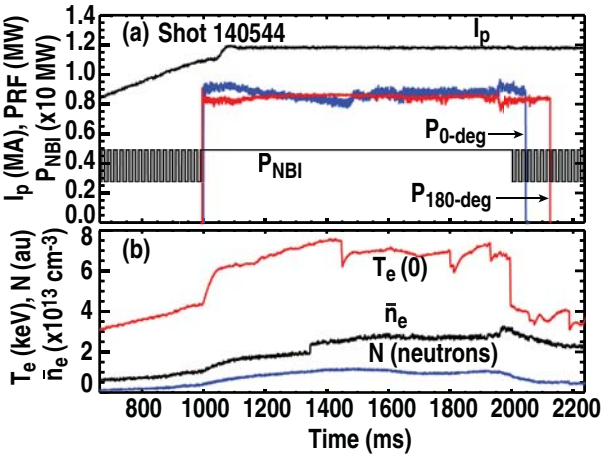

D.C. Pace Figure 1

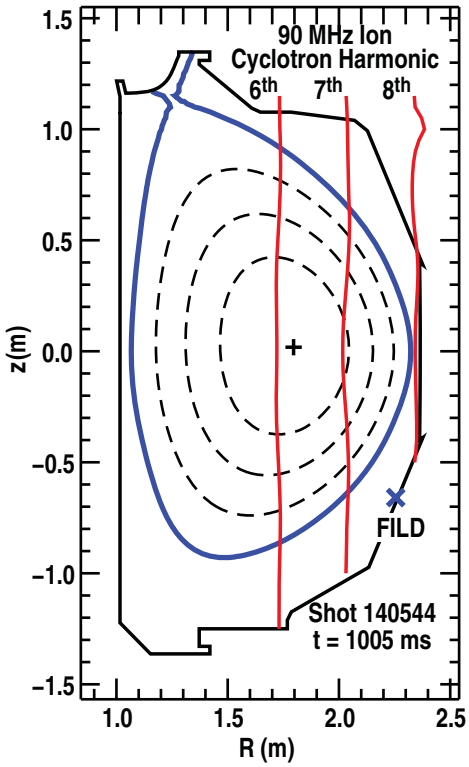

D.C. Pace Figure 2

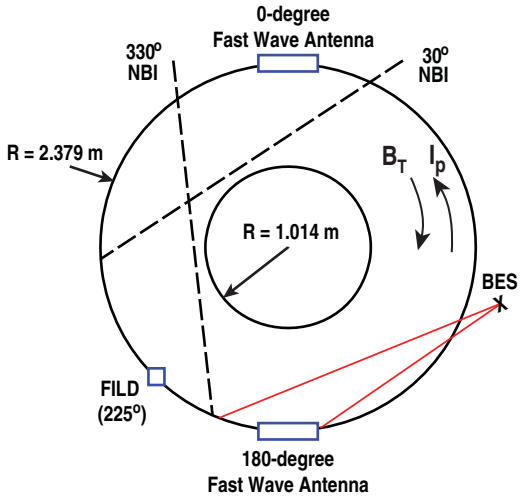

D.C. Pace Figure 3

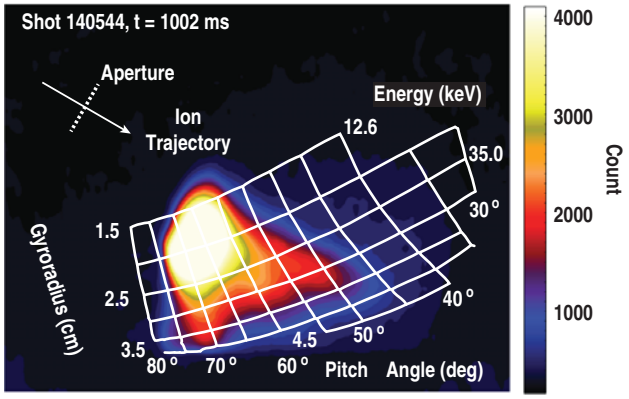

D.C. Pace Figure 4

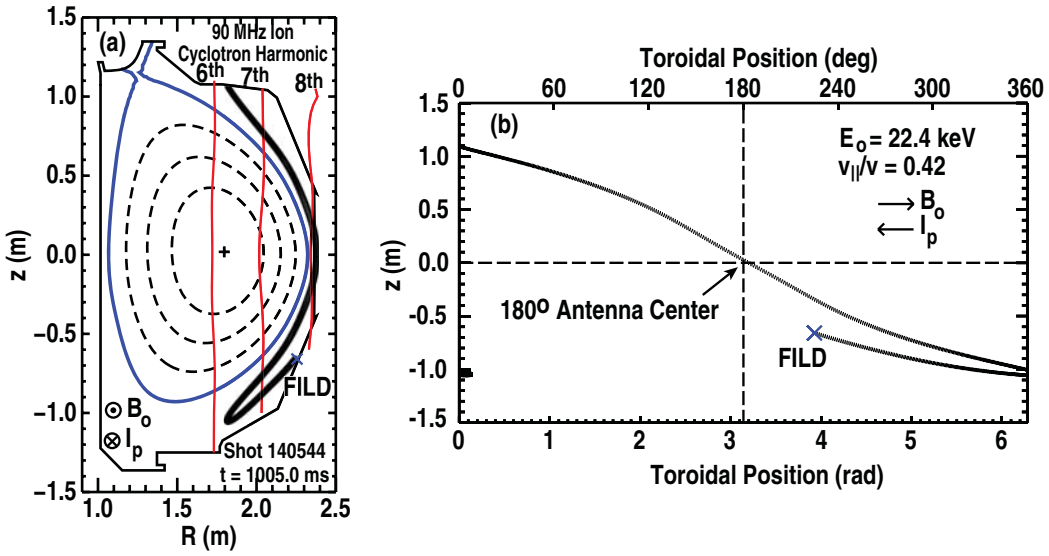

D.C. Pace Figure 5

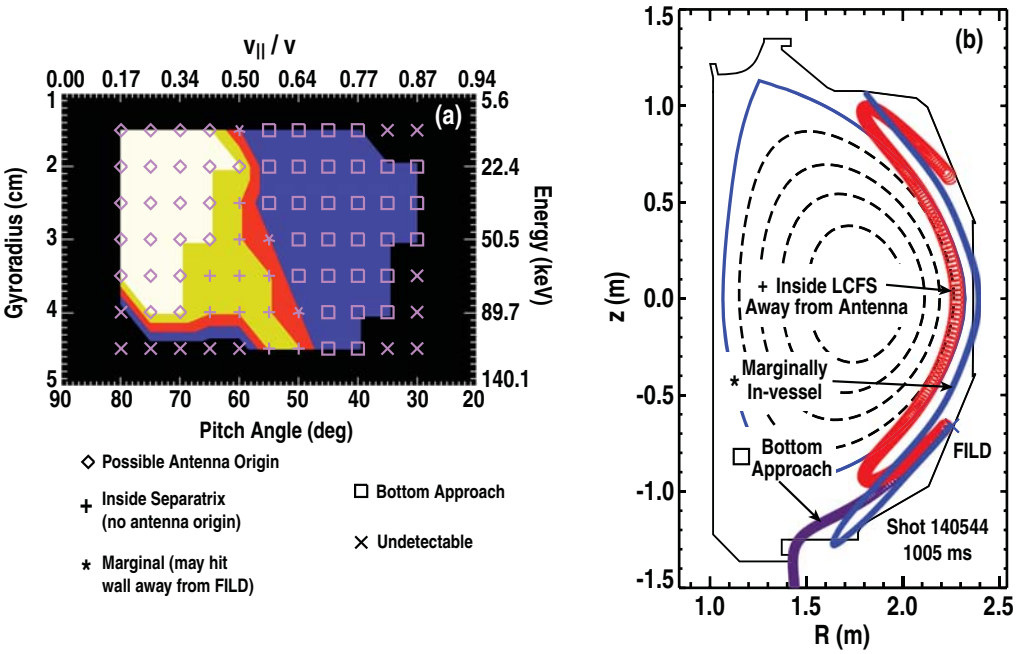

D.C. Pace Figure 6

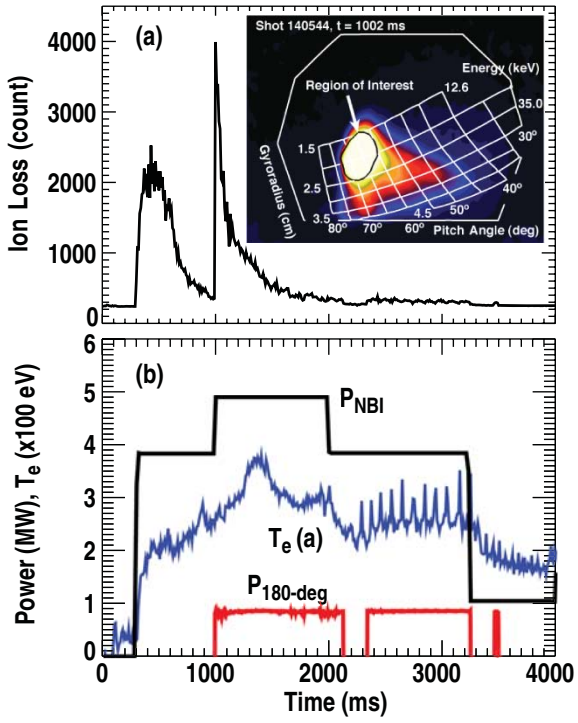

D.C. Pace Figure 7

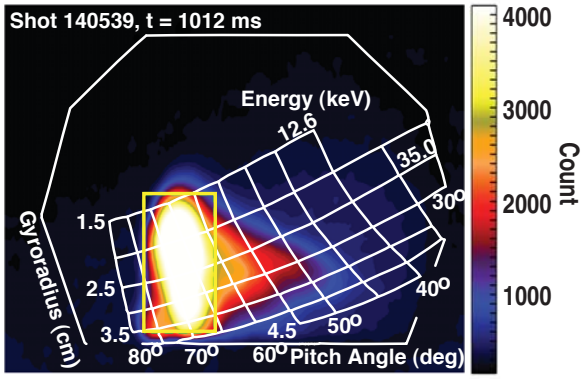

D.C. Pace Figure 8

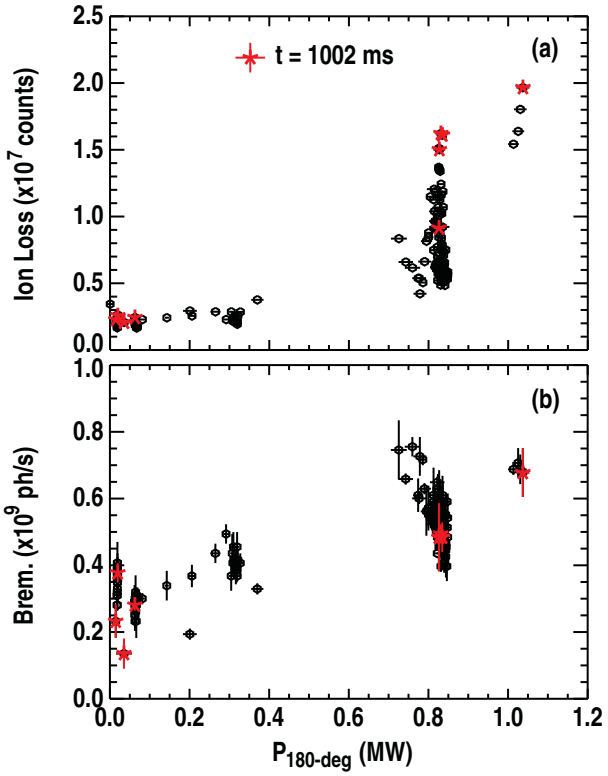

D.C. Pace Figure 9

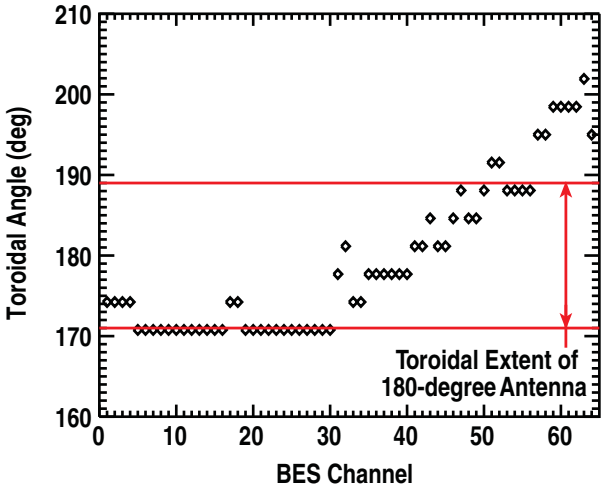

D.C. Pace Figure 10

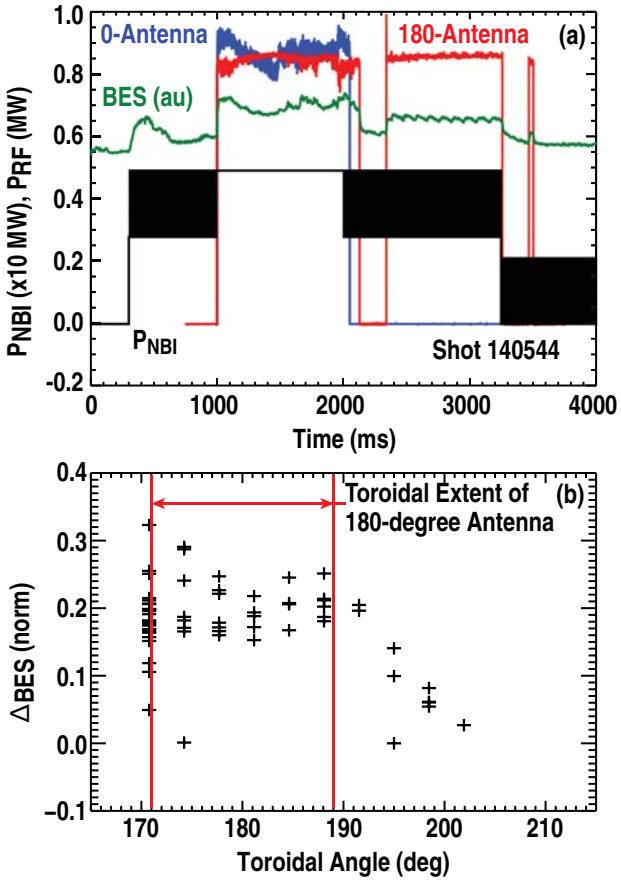

D.C. Pace Figure 11

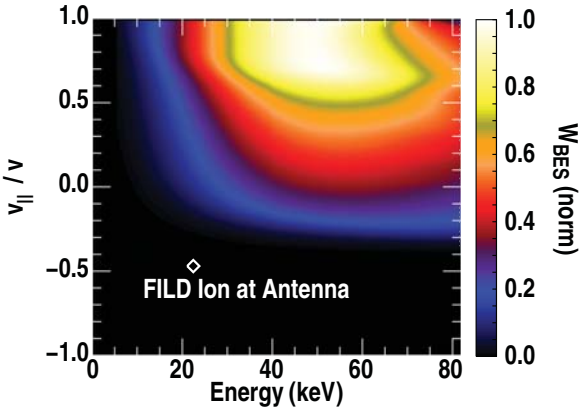

D.C. Pace Figure 12